science.sciencemag.org/content/370/6516/eabb5940/suppl/DC1

Supplementary Materials for

Atomic-scale microstructure of metal halide perovskite

Mathias Uller Rothmann, Judy S. Kim, Juliane Borchert, Kilian B. Lohmann, Colum M. O'Leary, Alex A. Sheader, Laura Clark, Henry J. Snaith, Michael B. Johnston, Peter D. Nellist*, Laura M. Herz*

*Corresponding author. Email: laura.herz@physics.ox.ac.uk (L.M.H.); peter.nellist@materials.ox.ac.uk (P.D.N.)

Published 30 October 2020, *Science* **370**, eabb5940 (2020)
DOI: 10.1126/science.abb5940

This PDF file includes:

Figs. S1 to S16
Table S1
References

Table S1: Overview of the imaging conditions for the images included in this manuscript.

Figure	Beam current	Dwell-time	Pixel size	Total dose per area per scan
1A-B	1.49 pA	1 µs	0.42 Å × 0.42 Å	53 e $Å^{-2}$
2A-C	1.49 pA	2 µs	0.53 Å × 0.53 Å	66 e $Å^{-2}$
3A-C	1.49 pA	2 µs	0.35 Å × 0.35 Å	152 e $Å^{-2}$
3D	1.49 pA	2 µs	0.29 Å × 0.29 Å	221 e $Å^{-2}$
4A,B,E,F	1.49 pA	2 µs	0.29 Å × 0.29 Å	221 e $Å^{-2}$
4C	1.49 pA	2 µs	0.42 Å × 0.42 Å	105 e $Å^{-2}$
4D	1.49 pA	2 µs	0.53 Å × 0.53 Å	66 e $Å^{-2}$
S2A-C	1.49 pA	1 µs	0.42 Å × 0.42 Å	53 e $Å^{-2}$
S3A-C	1.49 pA	2 µs	0.53 Å × 0.53 Å	66 e $Å^{-2}$
S4A	1.49 pA	1 µs	0.42 Å × 0.42 Å	53 e $Å^{-2}$
S5A-F	1.49 pA	2 µs	0.35 Å × 0.35 Å	152 e $Å^{-2}$
S7A-C	1.49 pA	2 µs	0.35 Å × 0.35 Å	152 e $Å^{-2}$
S7D	1.49 pA	2 µs	0.29 Å × 0.29 Å	221 e $Å^{-2}$
S9A-C	1.49 pA	2 µs	0.53 Å × 0.53 Å	66 e $Å^{-2}$
S12A-B	1.49 pA	2 µs	0.53 Å × 0.53 Å	66 e $Å^{-2}$
S13	1.49 pA	2 µs	0.53 Å × 0.53 Å	66 e $Å^{-2}$
S14A-C	1.49 pA	2 µs	0.29 Å × 0.29 Å	221 e $Å^{-2}$
S15A,B,E,F	1.49 pA	2 µs	0.29 Å × 0.29 Å	221 e $Å^{-2}$
S15C	1.49 pA	2 µs	0.42 Å × 0.42 Å	105 e $Å^{-2}$
S15D	1.49 pA	2 µs	0.53 Å × 0.53 Å	66 e $Å^{-2}$

Filtering

Butterworth filtering adds a low-pass filter across the Fourier transformation of the real-space image before reconstructing the image from the filtered FT, increasing the contrast of the image uniformly, as seen in Fig. S1B,E(*61, 62*). This approach makes it possible to retain information at grain boundaries, as seen on the left-hand side of Fig. S4B,E. All of the Butterworth-filtered images in this paper have been filtered using a 1st order filter.

Bragg filtering imposes a strict periodic mask on the Fourier transformation, only maintaining the signal from a selected set of spots in the FT, as seen in Fig. S1C,F(*63*). This process removes all signal not included in the spots, giving the highest signal-to-noise ratio. This makes the atomic structure very visible, but also removes any features not included in the mask, leading, for example, to weakening of grain boundary information, as seen in Fig. S4C: the right-hand grain has excellent contrast, but the left-hand grain is blurry from the filtering. Choosing the appropriate filtering is, therefore, essential in order for reliable information to be obtainable.

The film area imaged and displayed in Fig. S1A-C contains both pristine and damaged perovskite as evidenced by the chequered pattern most clearly seen in the top right corner of the filtered images, as well as the additional periodicity observed in the Fourier transformations.

LAADF multislice simulation

The multislice simulations were performed using the MUSTEM software(*64*, *65*) with a thickness of 30 nm and other parameters chosen to match the experimental LAADF acquisition. Aberrations were assumed to be negligible. The highly mobile FA^+ ion was modelled as a single particle, located at the notional carbon position with mean square displacements from the XRD literature(*66*). Multislice simulations are not able to quantitatively calculate the scattering intensity of the rotating FA^+ ions precisely and as a result, the intensity of the FA^+ columns in Fig. S4D and Fig. S10 is underestimated but the relative locations are correct. The brightness and contrast of the image were adjusted to clearly illustrate the geometry of the material, which however makes the Pb/I columns appear saturated

Geometric phase analysis (GPA) strain map

GPA strain mapping (Fig. S11) was done using the open-source Strain++ program written by Jon Peters(*67*) and based on the algorithm in ref. (*68*). The g-vectors were chosen to correspond to the 200_c and 020_c spots in the Fourier transform and the resulting ε_{xx} strain map was overlaid on the corresponding Butterworth-filtered LAADF image. The strain profile in Fig. S11 B was extracted from the strain map using Digital Micrograph.

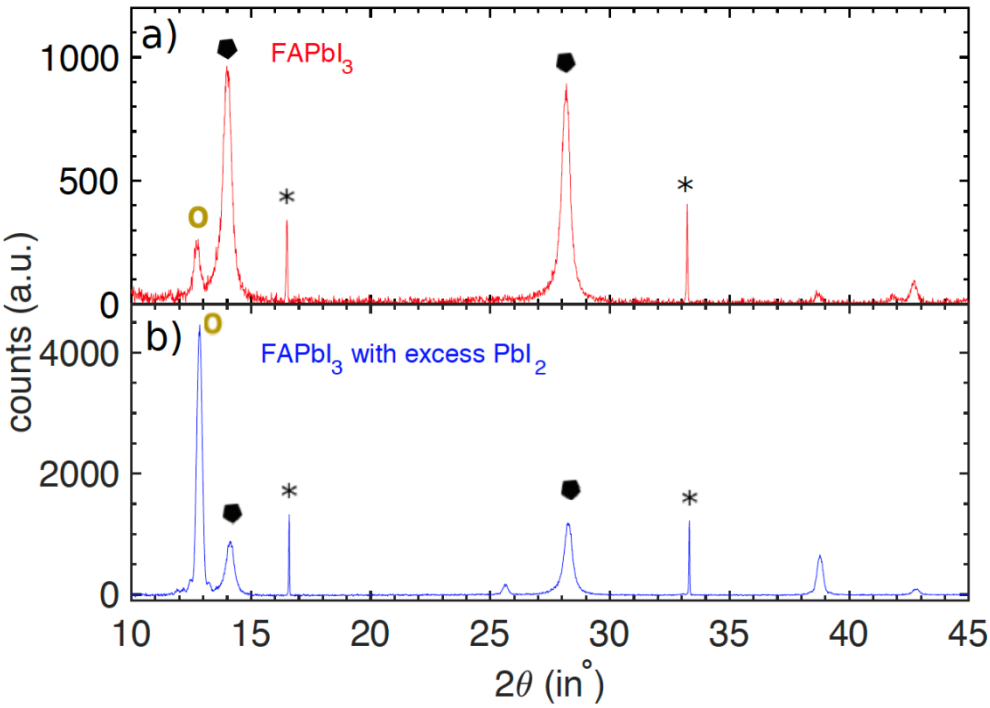

Fig. S1: X-ray diffraction patterns of $FAPbI_3$ films measured with a Panalytical X'pert powder diffractometer for (a) near-stoichiometric $FAPbI_3$ and (b) $FAPbI_3$ deposited under PbI_2-rich conditions. Thin-films were deposited from dual-source vapour protocols analogous to those described in the Methods section, but on quartz substrates which allowed for signal to be collected from areas larger than those defined by the copper TEM grids, and facilitated angle calibration with respect to the known quartz diffraction peaks (marked by stars). Film thicknesses were the same as those of the TEM samples. The background was subtracted from the spectra. The characteristic perovskite diffraction peaks (marked by black pentagons) are clearly visible near 14° and 28°. The near-stoichiometry $FAPbI_3$ film only exhibits a small PbI_2 diffraction peak (marked by beige circles) while the PbI_2-rich $FAPbI_3$ film fabricated with significant excess PbI_2 exhibits a much stronger PbI_2 peak.

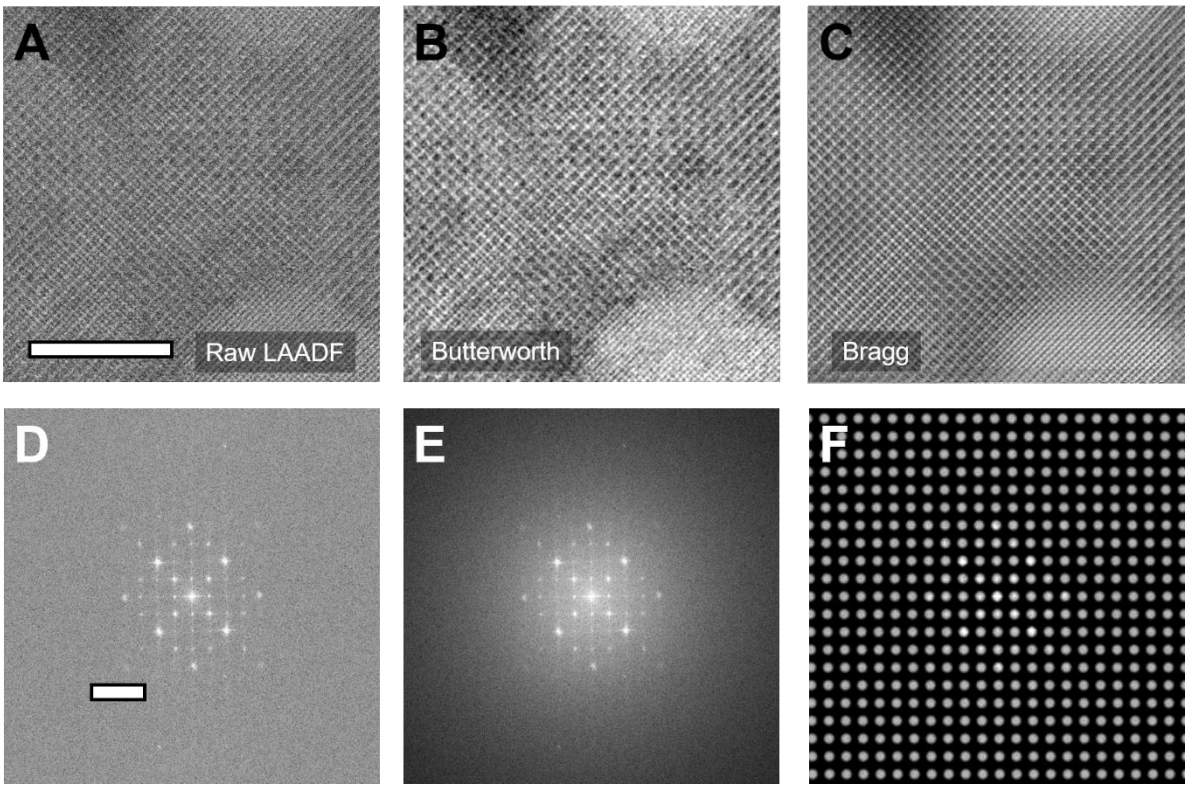

Fig. S2: Different filtering methods and their associated Fourier transformations. (A,D) show the raw LAADF image of an area of a $FAPbI_3$ thin film and its associated Fourier transformation, respectively. (B,E) show the same area and Fourier transformation after a Butterworth low-pass filter has been applied. (C,F) show the same area and Fourier transformation after a Bragg filter has been applied. The real-space scale bar represents 10 nm and applies to (A-C). The Fourier space scale bar represents 4 nm^{-1} and applies to (D-F).

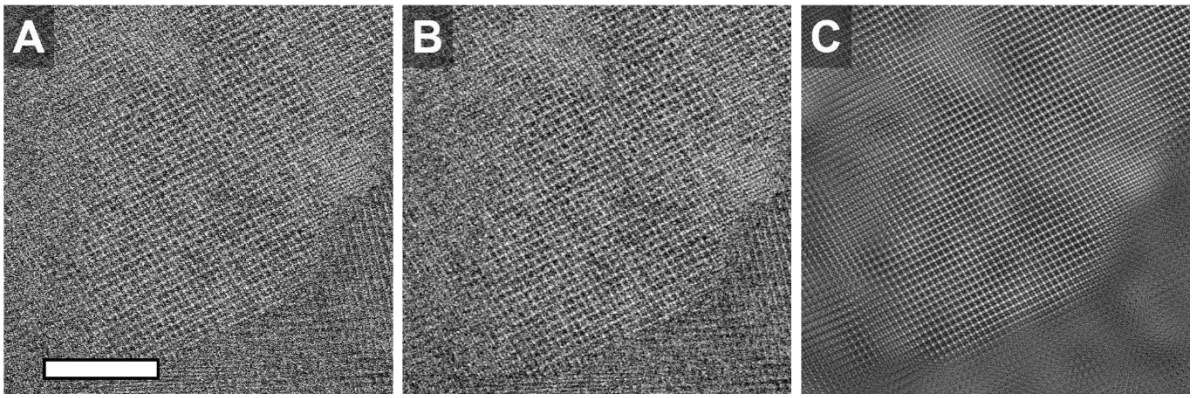

Fig. S3: Atomic-resolution HAADF micrographs of pristine PbI_2-rich $FAPbI_3$. (A) Raw data, (B) Butterworth filtered, (C) Bragg filtered. Images were obtained using a detector setting with 72.80 and 235.75 mrad as the inner and outer collection angles, respectively. The scale bar represents 10 nm.

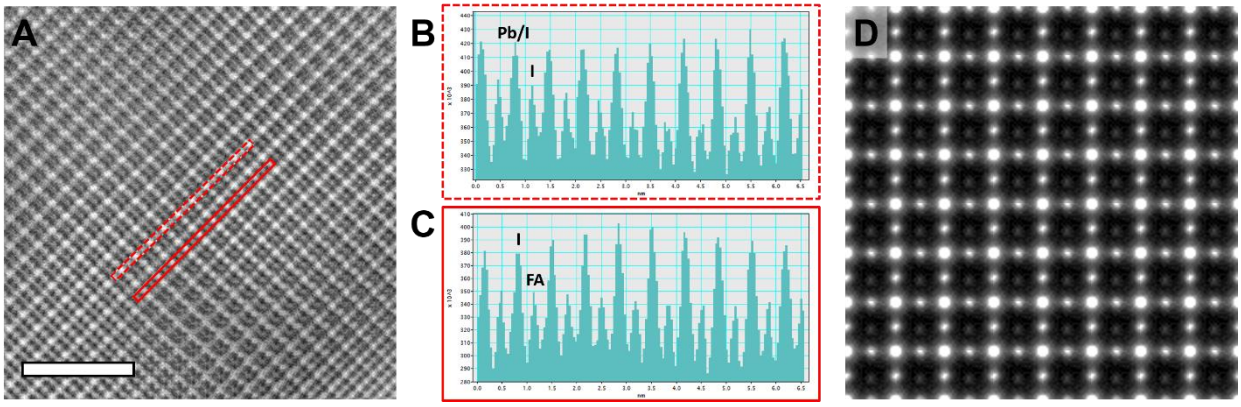

Fig. S4: Intensity line profiles across the Pb/I and the I/FA lattice sites. (A) shows a Bragg-filtered atomic resolution micrograph of a $FAPbI_3$ thin film similar to that displayed in Fig. 1 of the main manuscript. (B,C) show the intensity line profiles obtained from the dashed and solid rectangles in (A), respectively. The scale bar in (A) represents 5 nm. (D) Multislice simulation of the LAADF signal obtained from $FAPbI_3$ when using parameters chosen to match the experimental LAADF acquisition.

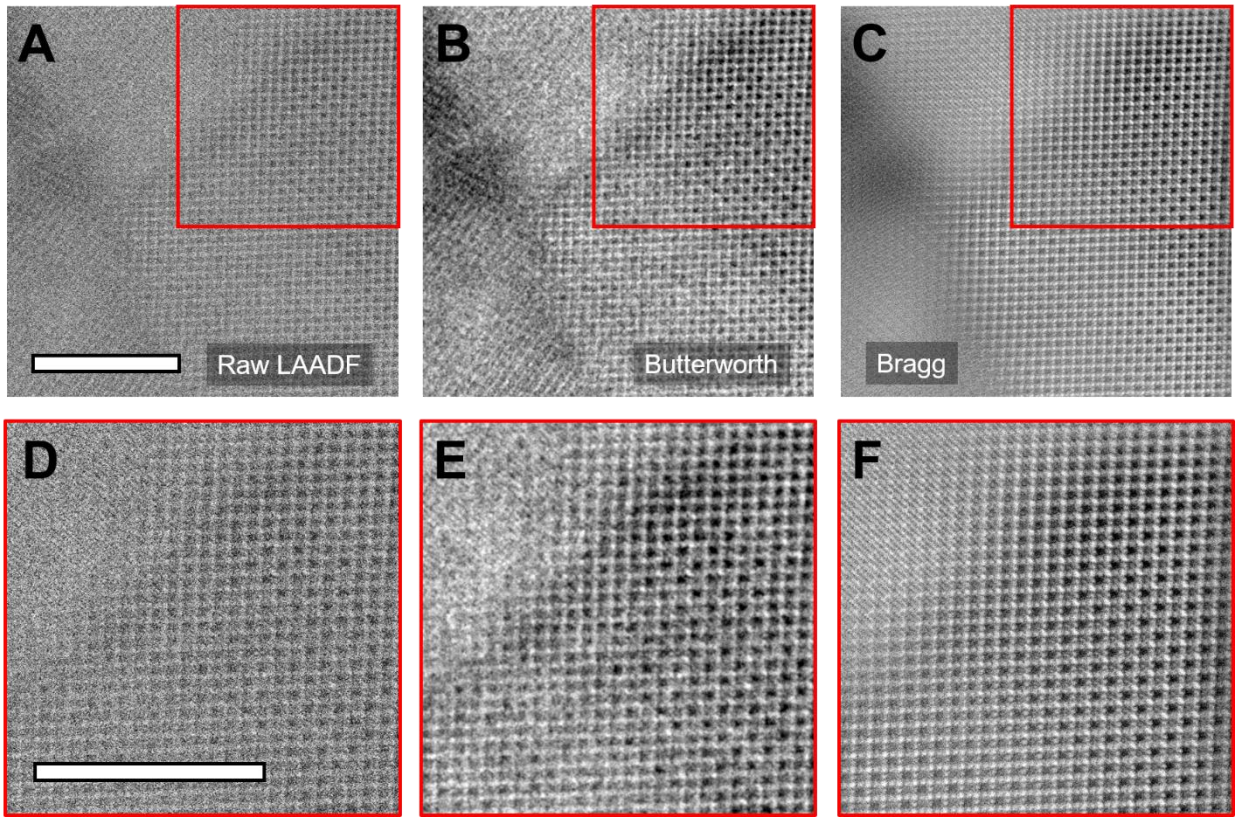

Fig. S5: Atomic-resolution LAADF micrographs of $FAPbI_3$ thin films prepared with excess PbI_2 showing a chequered intensity after mild radiation damage and seamless transitions between PbI_2 and $FAPbI_3$. (A-C) show real-space LAADF images of a $FAPbI_3$ thin film with (A) no filter applied, (B) a Butterworth low-pass filter applied, and (C) a Bragg filter applied. (D-F) show the corresponding areas marked in the red squares in (A-C). The raw LAADF images are noisy because of the low number of electrons used in order to minimise beam damage. Applying a Butterworth filter dramatically improves the signal-to-noise ratio, making grain boundaries evident. A Bragg filter further improves the signal-to-noise ratio, but does not maintain information from the grain boundaries. Both filters make the PbI_2-$FAPbI_3$ intergrowth in the top of the images visible, and the presence of the PbI_2 fringes in (F) confirms the close crystallographic relationship between the two phases. Both filters also make the chequered damage pattern in the right-hand grain very visible. The scale bars represent 10 nm.

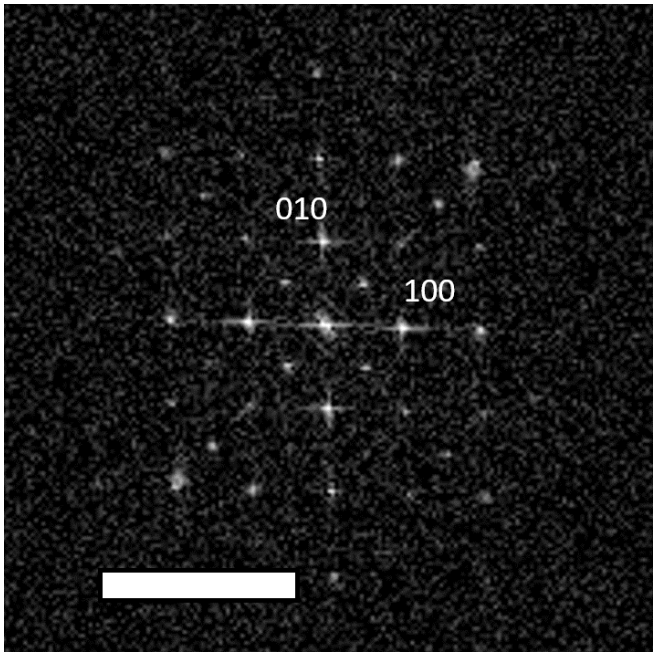

Fig. S6: Fourier transform of Fig. 3A. The scale bar represents 4 nm^{-1}.

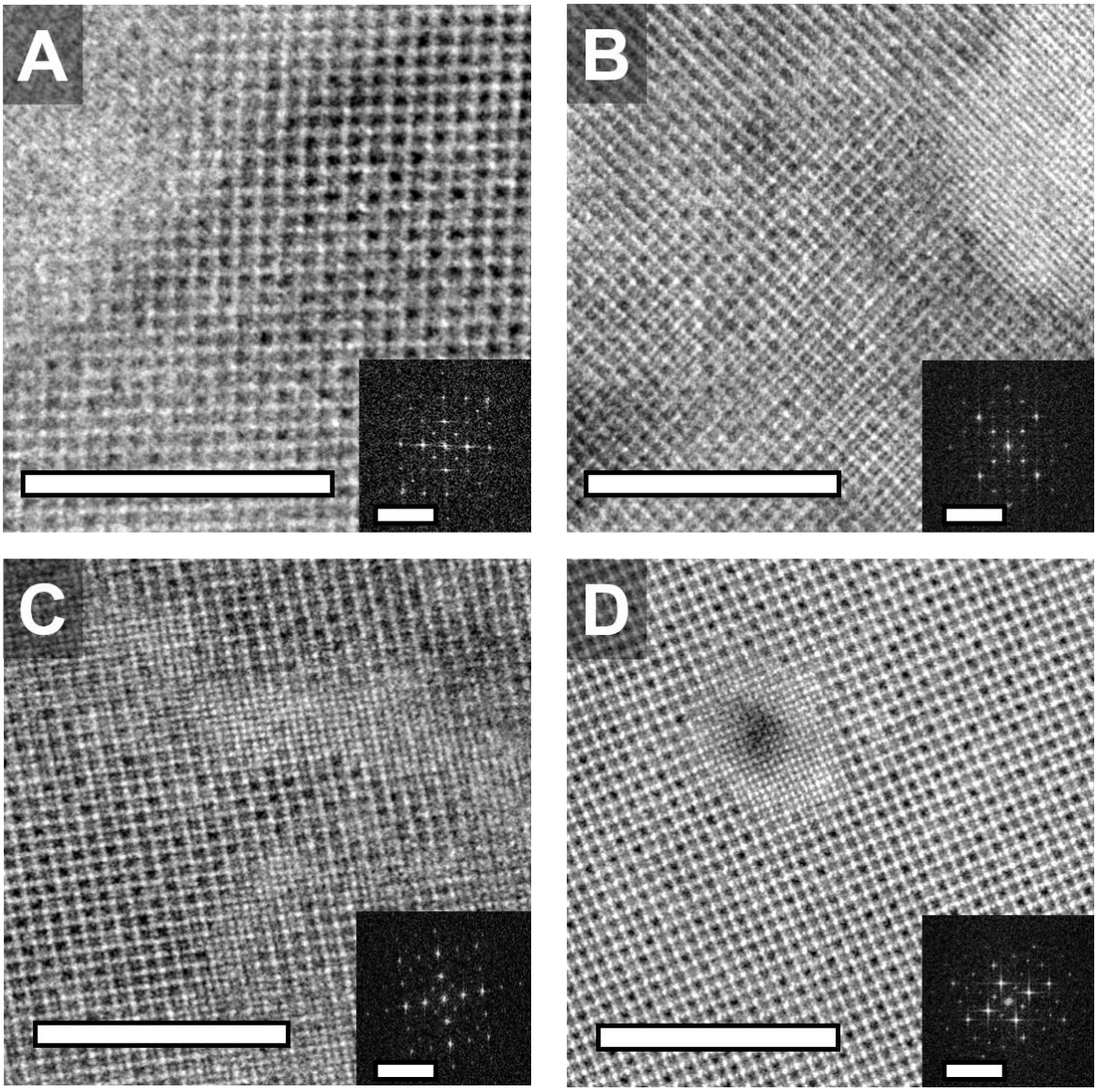

Fig. S7: Atomic-resolution LAADF micrographs of $FAPbI_3$ thin films showing undistorted transitions between PbI_2 and $FAPbI_3$, as well as a chequered intensity after mild radiation damage without colour overlay. All micrographs have been filtered using Butterworth filtering. (A-C) were prepared with significant excess PbI_2 and (D) is near-stoichiometric. The inserts show the Fourier transform of the real-space images, illustrating the epitaxial nature of the interfaces. The scale bars represent 10 nm in the real-space images and 4 nm^{-1} in the inserted Fourier transforms.

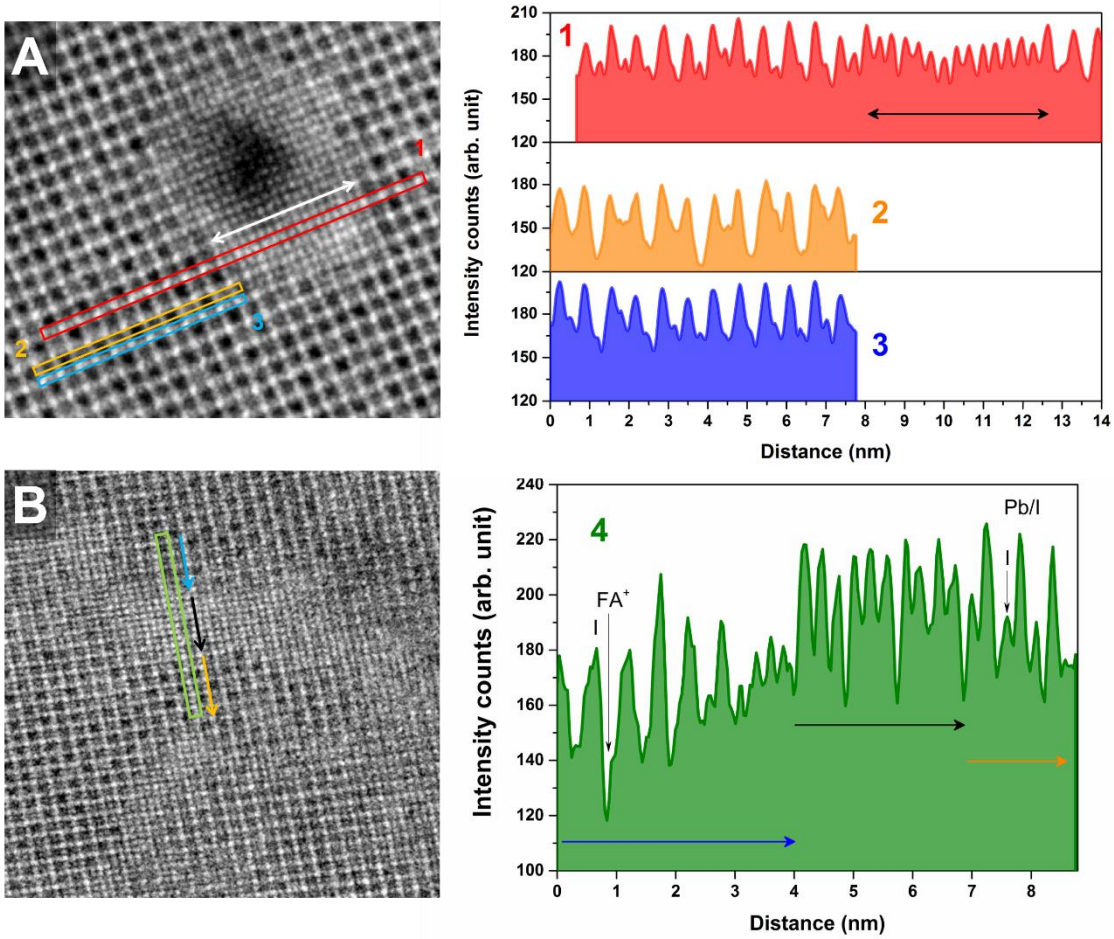

Fig. S8: Intensity line profiles of different atomic columns in $FAPbI_3$. (A) Line profile 1 (red) shows the intensity variation across Pb/I and I columns of damaged $FAPbI_3$ and the columns in the associated PbI_2. The intensity of the signal decreases within the PbI_2 region (marked by the black and white arrows), indicating a local loss of material. Line profile 2 (yellow) shows the ordering of the FA^+ columns with every other column being either partially or fully empty, indicating a columnar redistribution of the FA^+ after beam damage. Line profile 3 (blue) shows minimal evidence of ordered loss of I^-, suggesting that the $[PbI_6]$ octahedral units can remain intact in the perovskite lattice despite the loss of FA^+. (B) Line profile 4 (green) shows the intensity variation across the perovskite/PbI_2 intergrowth causing half a unit cell shit, displayed in Fig. 3C. The LAADF signal intensity of the FA^+/I columns (blue arrow) is lower than that of the I/Pb:I columns (orange arrow), illustrating the shift of half a unit cell across the PbI_2 (black arrow). The composition of the film imaged in (A) is near-stoichiometric, and in (B) as prepared with significant excess PbI_2.

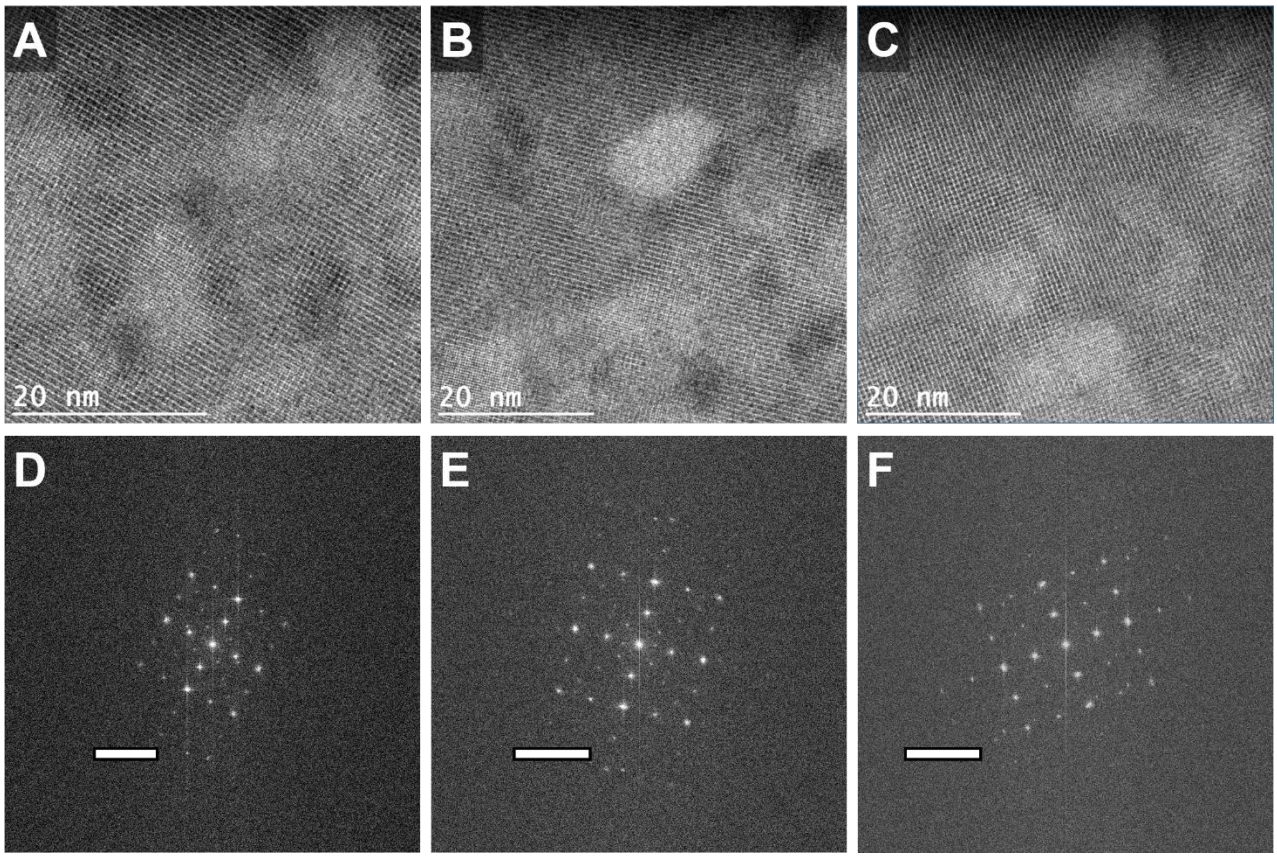

Figure S9: PbI_2 incorporation into $FAPbI_3$ prepared with significant excess PbI_2. (A-C) Representative Butterworth-filtered LAADF micrographs showing coherent incorporation of PbI_2 clusters into the surrounding perovskite lattice. (D-F) Fourier transforms of the micrographs taken before Butterworth filtering, showing only a single pattern in each transform, indicating that the PbI_2 is incorporated epitaxially into the perovskite lattice in all directions. The scale bars in (D-F) represent 4 nm^{-1}.

$FAPbI_3$ / PbI_2 interface

The structure of PbI_2 comprises [PbI_6] octahedra that form 2D layers which interact through van der Waals forces with neighbouring layers. The I-I distance across the PbI_2 octahedra (0.64 nm(*45*)) is very close to the corresponding distance in the similar octahedra in $FAPbI_3$ (0.63 nm). The structure of the 2H polytype viewed along [110] is shown in the top of Fig. S10.

The weak van der Waals interaction between layers leads to extensive polytypism in PbI_2 corresponding to various shifts between the layers. The bottom of Fig. S10 shows how a small shift in the registration of the layers and a slight compression of the gap between the layers can lead to a structure that is epitaxial and coherent with the cubic perovskite structure with the [PbI_6] octahedra being continuous across the two structures.

This interpretation of the interface structure also explains the relative intensities of the atomic columns in the images in Fig. 3 and Fig. S8. The most intense columns are those in the perovskite with the atomic sequence I-Pb-I-Pb-I-Pb-I. The next most intense columns are those in the PbI_2 phase that follow the sequence I-Pb-I-_-I-Pb-I where the underscore is the gap between the layers. They have consistent intensity in both the 2H structure and the distorted epitaxial structure in Fig 2 consistent with our model. The I-_-I-_-I columns in the perovskite follow in the weakening intensity sequence with finally the FA columns being the weakest.

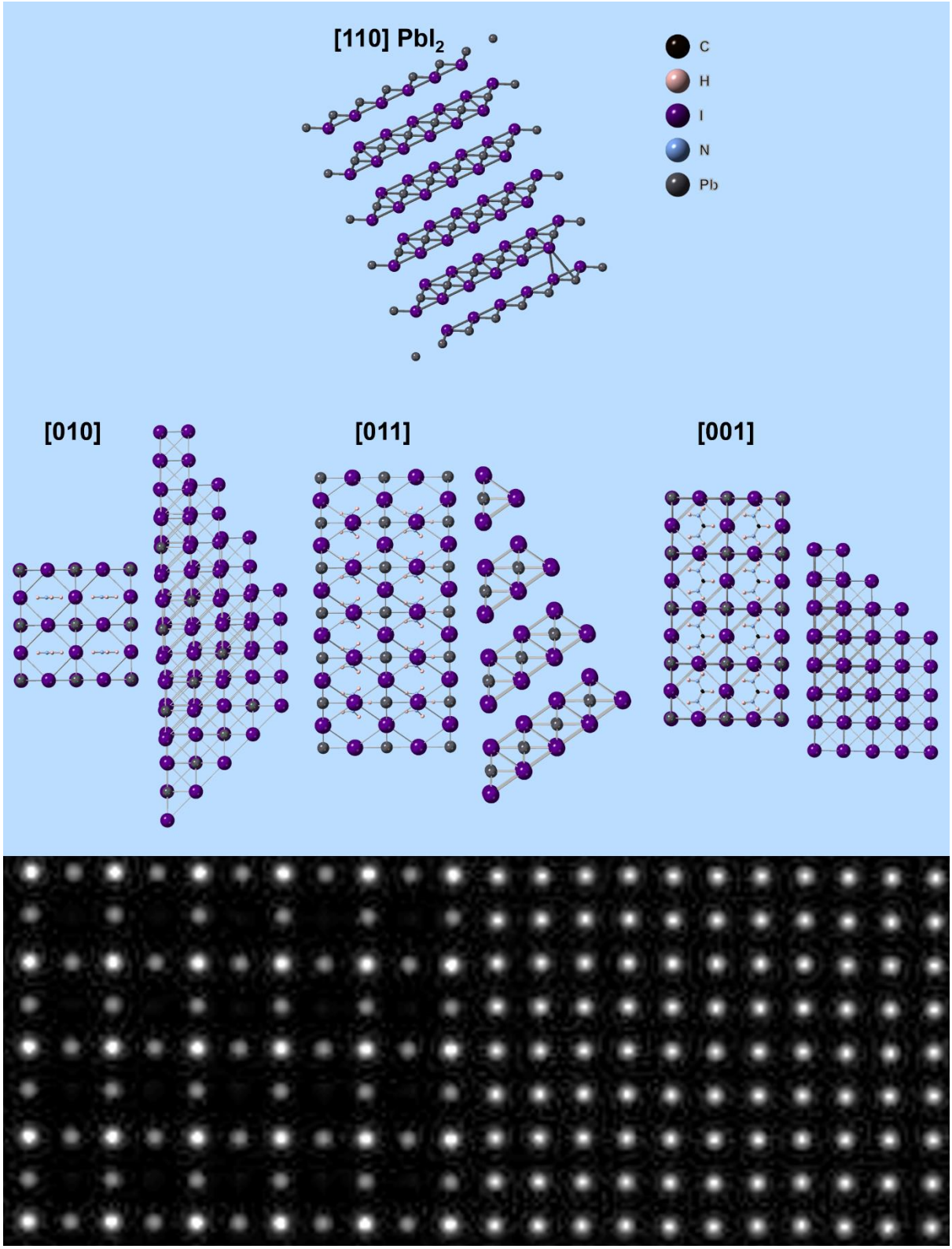

Fig. S10: Stick and ball model of the interface between $FAPbI_3$ and slightly modified 2H PbI_2 as well as LAADF signal intensity simulation of the interface. Top shows [100]-oriented 2H PbI_2. Middle shows the interface between $FAPbI_3$ and PbI_2. The interface is shown in three different orientations, with the orientation index corresponding to the $FAPbI_3$ orientation. The perovskite structure is displayed on the left and the PbI_2 on the right of each interface. Bottom shows the simulated LAADF signal intensity across the interface along the perovskite <100> axis, with the perovskite on the left and PbI_2 on the right. The low intensity

of the FA^+ columns caused by the multislice simulations being unable to quantitatively calculate the scattering intensity of the rotating FA^+ ions precisely.

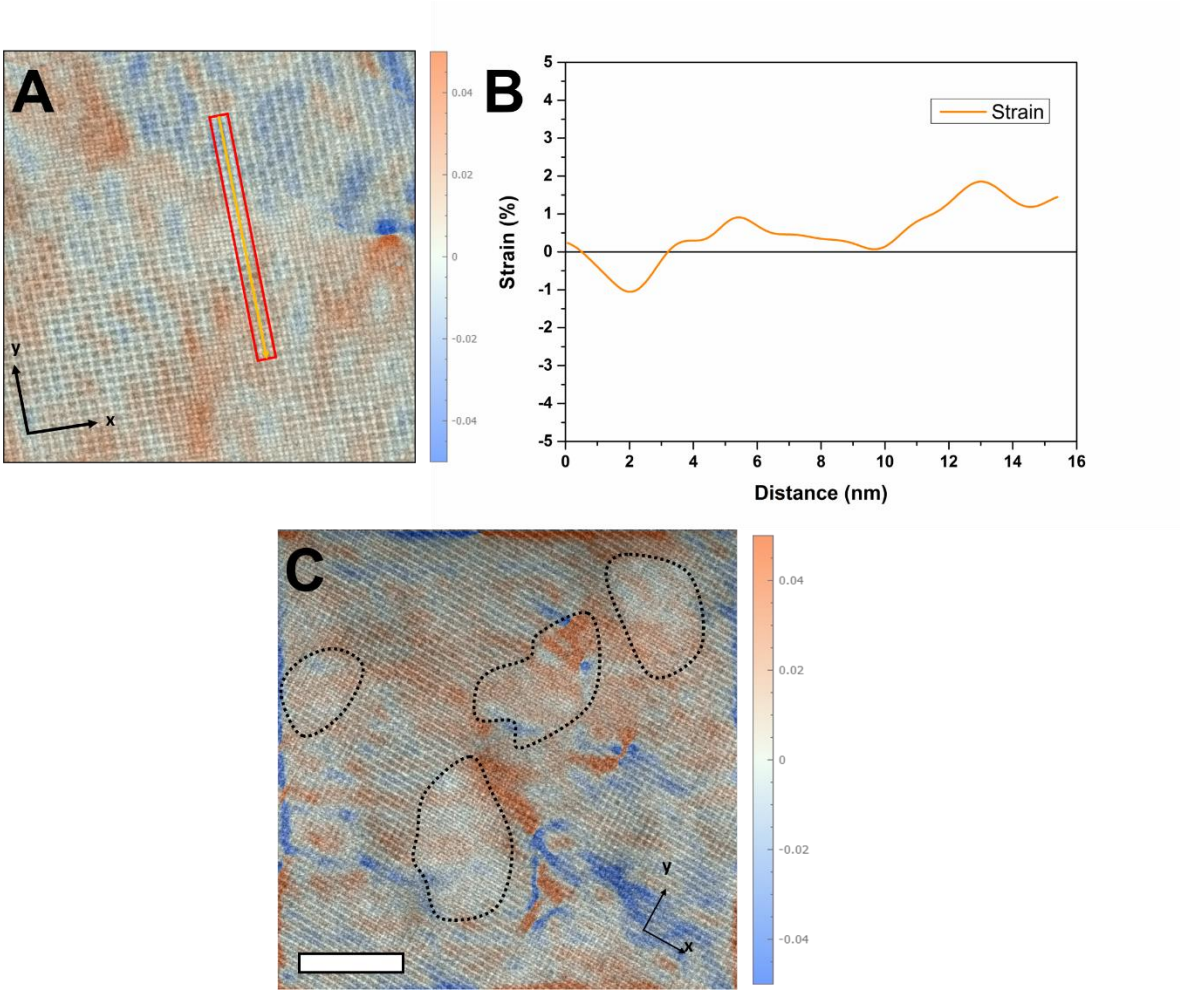

Fig. S11: Crystallographic strain across a PbI_2/$FAPbI_3$ interface. (A) Geometric phase analysis heat map of the ε_{xx} strain showing virtually no strain associated with the interface. (B) Line profile of the strain within the red rectangle along the orange arrow. The strain across the interface varies from -1 % to 2 %. (C) Geometric strain analysis heat map of the ε_{yy} strain map in the pristine PbI_2-rich $FAPbI_3$ film displayed in Fig. 9A, showing some atomic strain throughout the film. Some PbI_2 inclusions are highlighted by the dotted lines, showing that there is no inherently higher strain associated with the PbI_2/$FAPbI_3$ interface than within the rest of the film. The scale bar represents 10 nm.

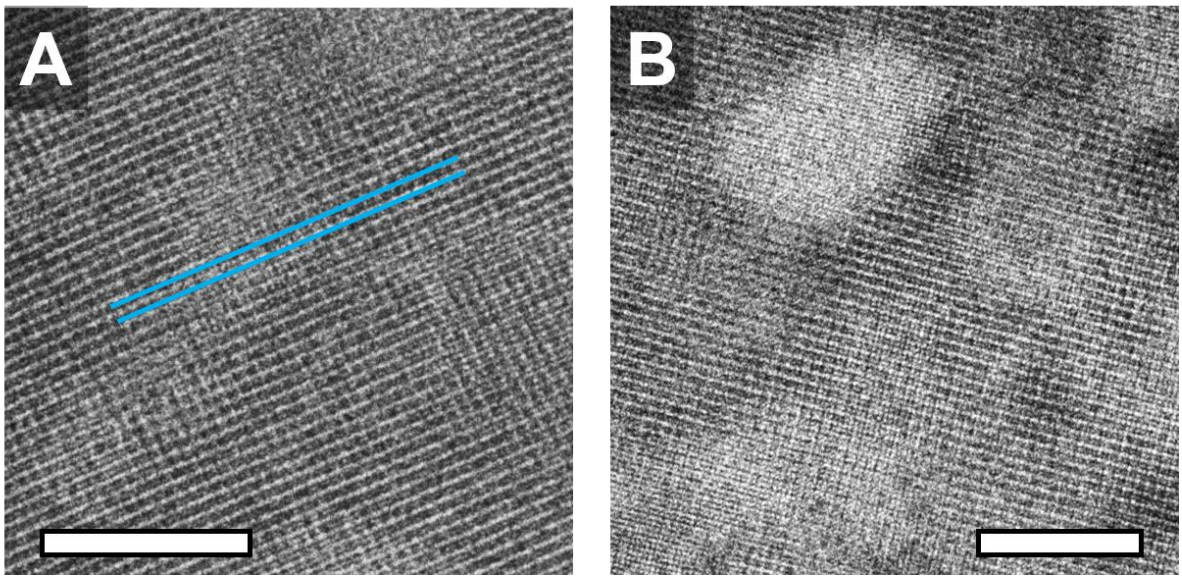

Fig. S12: Atomic-resolution LAADF micrographs of pristine PbI_2-rich $FAPbI_3$ showing (A) shift of half a perovskite unit cell in pristine $FAPbI_3$ and (B) PbI_2 intergrowth with the pristine perovskite lattice. The scale bars represent 10 nm.

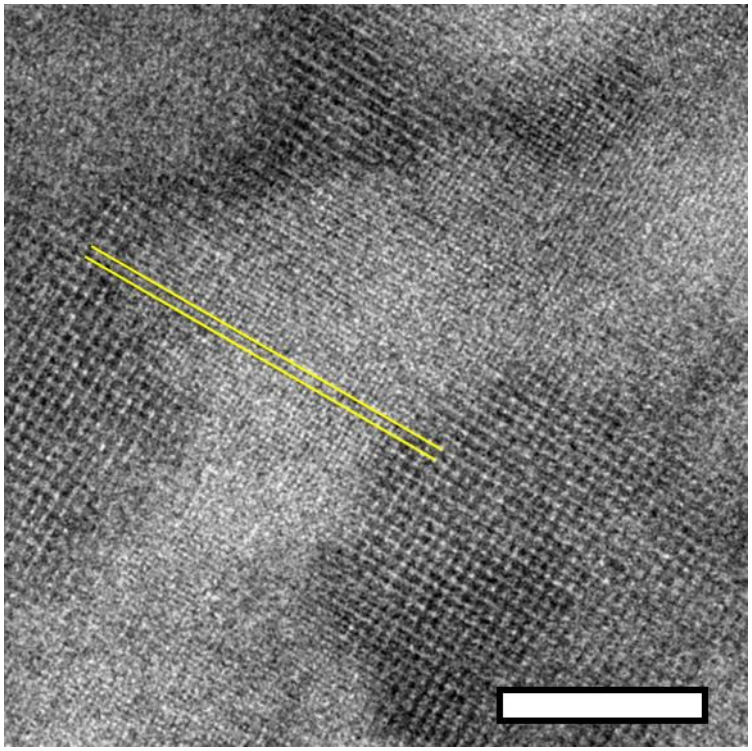

Fig. S13: Atomic-resolution LAADF micrograph of PbI_2-rich $MAPbI_3$ showing both the undistorted perovskite-to-PbI_2 transitions and the shift of half a unit cell across a PbI_2 region (parallel yellow lines). The scale bar represents 10 nm.

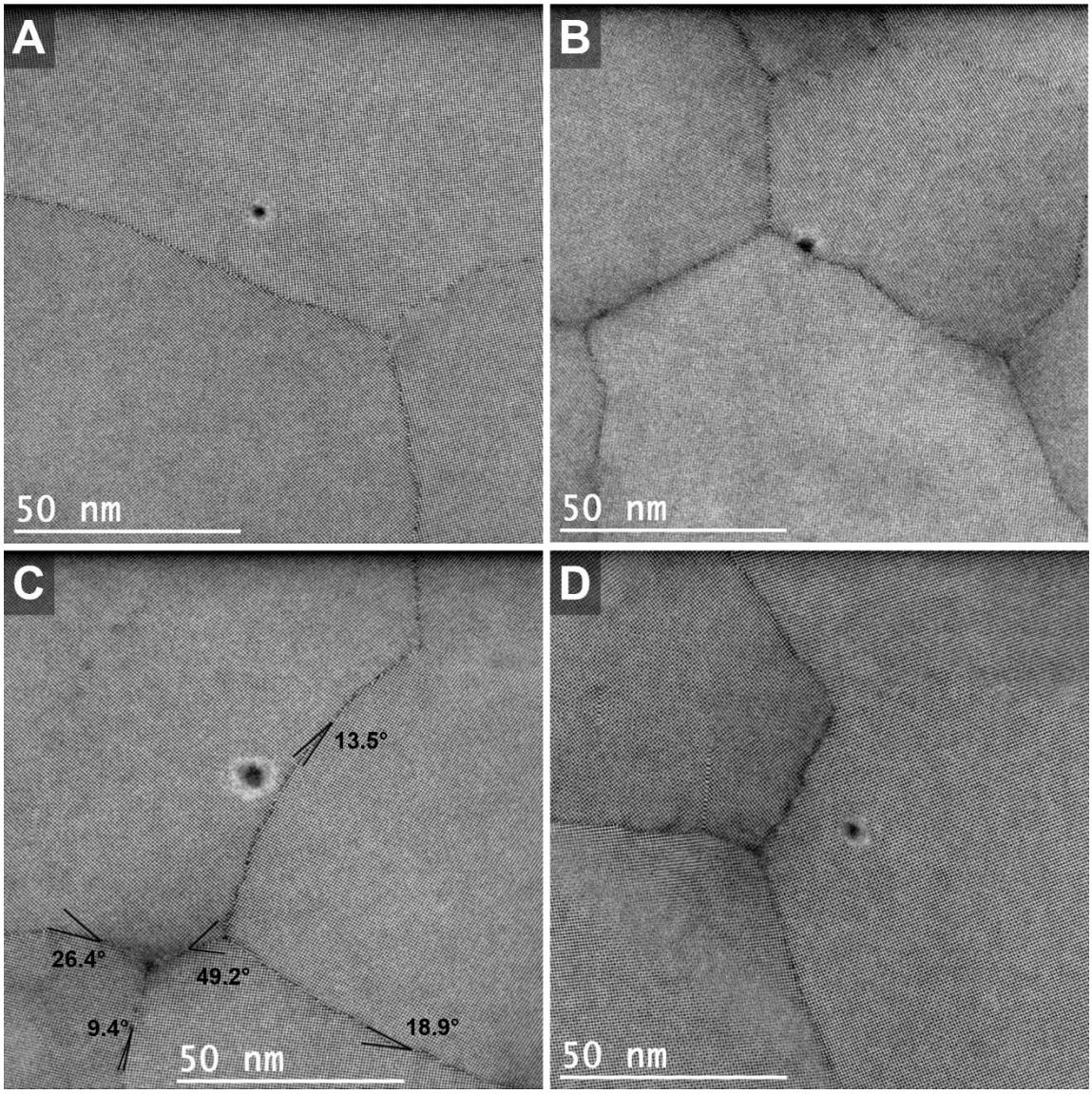

Fig. S14: Representative lower-magnification Butterworth-filtered atomic-resolution micrographs of $FAPbI_3$ grains as seen in a 30-nm thick film prepared near the correct stoichiometry. The round dark areas are regions damaged by the parked electron beam before image acquisition. Fig. 4A in the main manuscript is a magnified excerpt of (A), Fig. 4B is a magnified excerpt of (C), and Fig. 3D and Fig. 4E are magnified excerpts of (D). A wide range of grain boundary angles are evident in (C), illustrating the highly conformal nature of $FAPbI_3$.

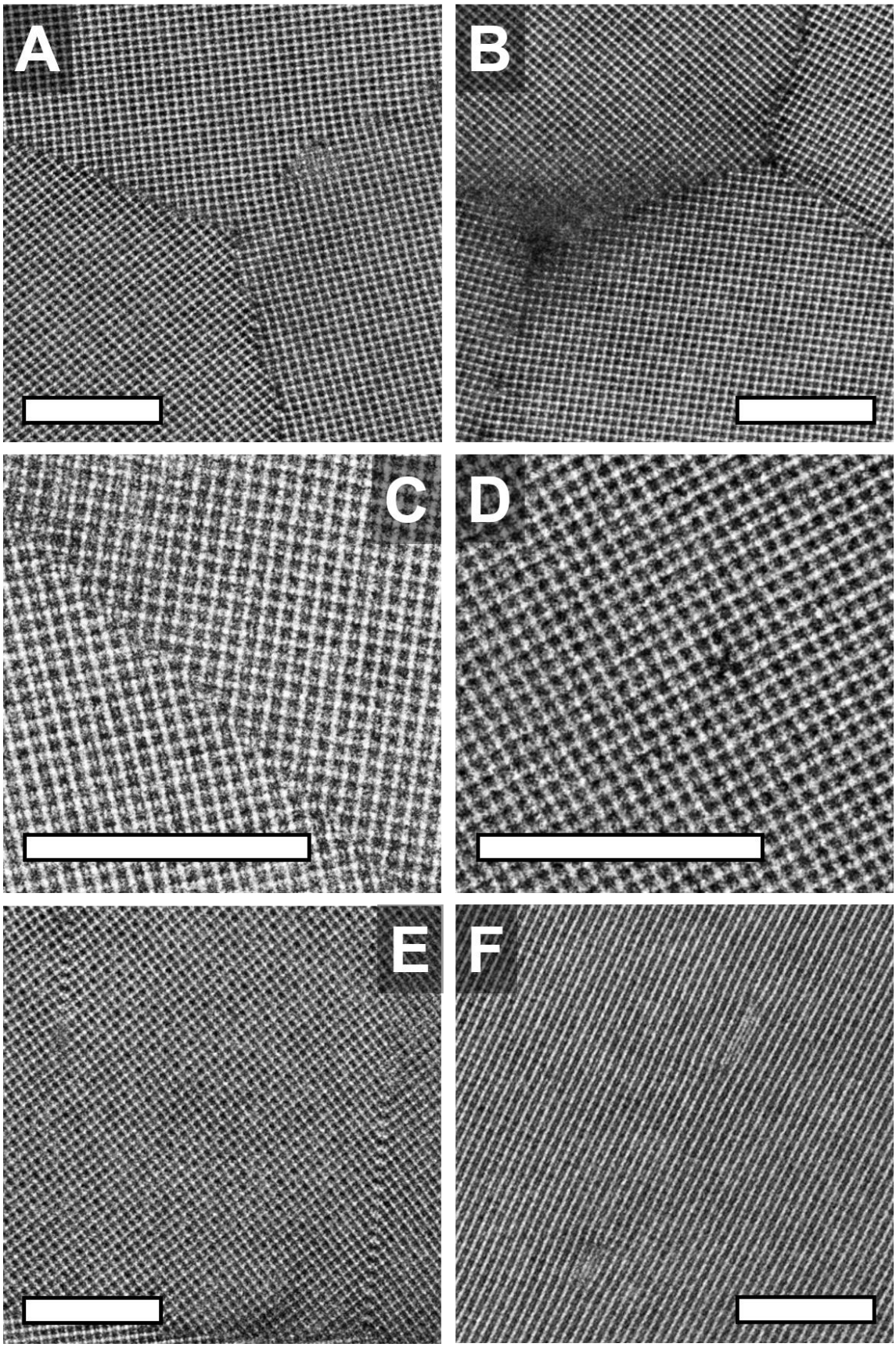

Fig. S15: Butterworth-filtered atomic-resolution micrographs of representative $FAPbI_3$ grain boundaries and crystal defects as seen in a 30-nm thick film prepared near the correct stoichiometry, shown without colour overlay. The scale bars represent 10 nm.

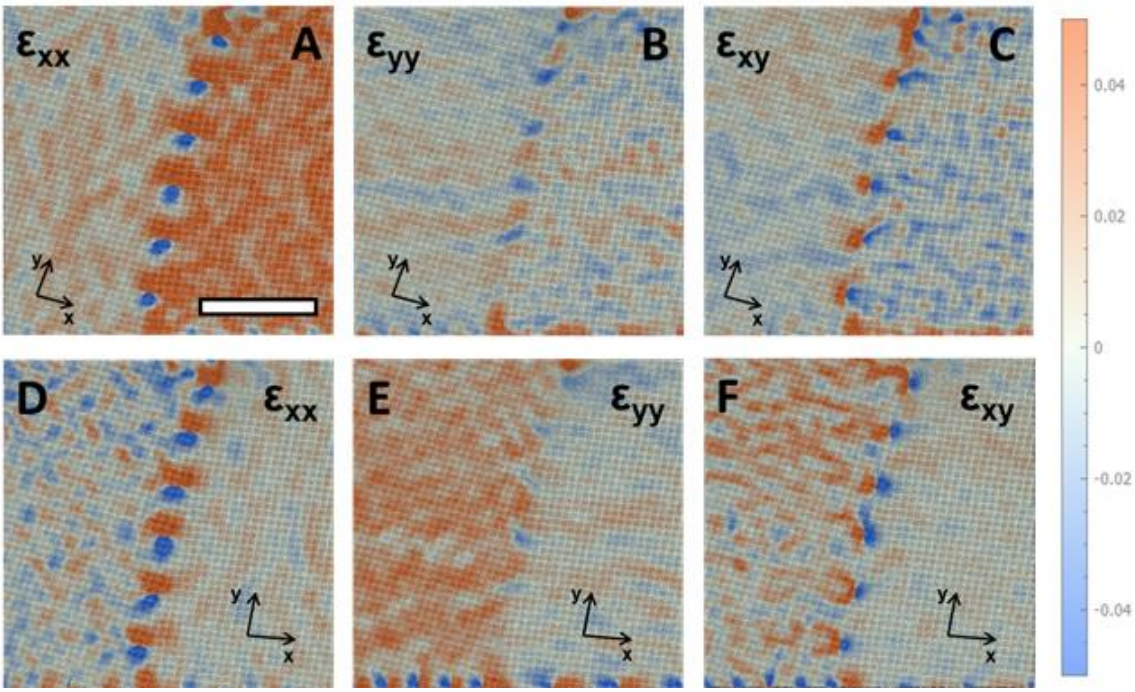

Fig. S16: GPA strain maps near the low-angle boundary between two near-stoichiometric $FAPbI_3$ grains displayed in the bottom left of Fig. 4B. (A-C) show the xx, yy, and xy strain in the left-hand grain, and (D-F) show the xx, yy, and xy strain in the right-hand grain, respectively. A periodic pattern of xx and xy strain with alternating sign is evident and arises from the periodic array of edge dislocations forming the grain boundary, whereas the yy strain (lying close to perpendicular to the dislocation burgers vectors) is much lower at the boundary. All significant strain is localised to within one or two unit cells from the boundary, showing that the boundary does not induce long-range strain in the grains themselves. The inserted coordinate axes show the respective defined lattice directions. The periodic strain patterns at the bottom of each image are due to edge effects and are not physical. The scale bar represents 10 nm and applies to all the images.

References

1. H.-S. Kim, C.-R. Lee, J.-H. Im, K.-B. Lee, T. Moehl, A. Marchioro, S.-J. Moon, R. Humphry-Baker, J.-H. Yum, J. E. Moser, M. Grätzel, N.-G. Park, Lead iodide perovskite sensitized all-solid-state submicron thin film mesoscopic solar cell with efficiency exceeding 9%. *Sci. Rep.* **2**, 591 (2012). doi:10.1038/srep00591 Medline

2. M. Liu, M. B. Johnston, H. J. Snaith, Efficient planar heterojunction perovskite solar cells by vapour deposition. *Nature* **501**, 395–398 (2013). doi:10.1038/nature12509 Medline

3. H. Zhou, Q. Chen, G. Li, S. Luo, T. B. Song, H.-S. Duan, Z. Hong, J. You, Y. Liu, Y. Yang, Interface engineering of highly efficient perovskite solar cells. *Science* **345**, 542–546 (2014). doi:10.1126/science.1254050 Medline

4. N. J. Jeon, J. H. Noh, Y. C. Kim, W. S. Yang, S. Ryu, S. I. Seok, Solvent engineering for high-performance inorganic-organic hybrid perovskite solar cells. *Nat. Mater.* **13**, 897–903 (2014). doi:10.1038/nmat4014 Medline

5. J.-P. Correa-Baena, A. Abate, M. Saliba, W. Tress, T. Jesper Jacobsson, M. Grätzel, A. Hagfeldt, The rapid evolution of highly efficient perovskite solar cells. *Energy Environ. Sci.* **10**, 710–727 (2017). doi:10.1039/C6EE03397K

6. M. Saliba, T. Matsui, K. Domanski, J.-Y. Seo, A. Ummadisingu, S. M. Zakeeruddin, J.-P. Correa-Baena, W. R. Tress, A. Abate, A. Hagfeldt, M. Grätzel, Incorporation of rubidium cations into perovskite solar cells improves photovoltaic performance. *Science* **354**, 206–209 (2016). doi:10.1126/science.aah5557 Medline

7. D. P. McMeekin, G. Sadoughi, W. Rehman, G. E. Eperon, M. Saliba, M. T. Hörantner, A. Haghighirad, N. Sakai, L. Korte, B. Rech, M. B. Johnston, L. M. Herz, H. J. Snaith, A mixed-cation lead mixed-halide perovskite absorber for tandem solar cells. *Science* **351**, 151–155 (2016). doi:10.1126/science.aad5845 Medline

8. D. W. deQuilettes, W. Zhang, V. M. Burlakov, D. J. Graham, T. Leijtens, A. Osherov, V. Bulović, H. J. Snaith, D. S. Ginger, S. D. Stranks, Photo-induced halide redistribution in organic-inorganic perovskite films. *Nat. Commun.* **7**, 11683 (2016). doi:10.1038/ncomms11683 Medline

9. C. C. Stoumpos, C. D. Malliakas, M. G. Kanatzidis, Semiconducting tin and lead iodide perovskites with organic cations: Phase transitions, high mobilities, and near-infrared photoluminescent properties. *Inorg. Chem.* **52**, 9019–9038 (2013). doi:10.1021/ic401215x Medline

10. T. Baikie, N. S. Barrow, Y. Fang, P. J. Keenan, P. R. Slater, R. O. Piltz, M. Gutmann, S. G. Mhaisalkar, T. J. White, A combined single crystal neutron/X-ray diffraction and solid-state nuclear magnetic resonance study of the hybrid perovskites $CH_3NH_3PbX_3$ (X= I, Br and Cl). *J. Mater. Chem. A* **3**, 9298–9307 (2015). doi:10.1039/C5TA01125F

11. M. U. Rothmann, W. Li, J. Etheridge, Y. B. Cheng, Microstructural Characterisations of Perovskite Solar Cells—From Grains to Interfaces: Techniques, Features, and Challenges. *Adv. Energy Mater.* **7**, 1700912 (2017). doi:10.1002/aenm.201700912

12. K. Domanski, E. A. Alharbi, A. Hagfeldt, M. Grätzel, W. Tress, Systematic investigation of the impact of operation conditions on the degradation behaviour of perovskite solar cells. *Nat. Energy* **3**, 61–67 (2018). doi:10.1038/s41560-017-0060-5

13. L. Hong, Y. Hu, A. Mei, Y. Sheng, P. Jiang, C. Tian, Y. Rong, H. Han, Improvement and Regeneration of Perovskite Solar Cells via Methylamine Gas Post-Treatment. *Adv. Funct. Mater.* **27**, 1703060 (2017). doi:10.1002/adfm.201703060

14. D. H. Cao, C. C. Stoumpos, C. D. Malliakas, M. J. Katz, O. K. Farha, J. T. Hupp, M. G. Kanatzidis, Remnant PbI_2, an unforeseen necessity in high-efficiency hybrid perovskite-based solar cells? *APL Mater.* **2**, 091101 (2014). doi:10.1063/1.4895038

15. H.-Y. Hsu, L. Ji, M. Du, J. Zhao, E. T. Yu, A. J. Bard, Optimization of PbI_2/$MAPbI_3$ perovskite composites by scanning electrochemical microscopy. *J. Phys. Chem. C* **120**, 19890–19895 (2016). doi:10.1021/acs.jpcc.6b07850

16. Y. C. Kim, N. J. Jeon, J. H. Noh, W. S. Yang, J. Seo, J. S. Yun, A. Ho-Baillie, S. Huang, M. A. Green, J. Seidel, T. K. Ahn, S. I. Seok, Beneficial effects of PbI_2 incorporated in organo-lead halide perovskite solar cells. *Adv. Energy Mater.* **6**, 1502104 (2016). doi:10.1002/aenm.201502104

17. J.-W. Lee, S.-H. Bae, N. De Marco, Y.-T. Hsieh, Z. Dai, Y. Yang, The role of grain boundaries in perovskite solar cells. *Mater. Today Energy* **7**, 149–160 (2018). doi:10.1016/j.mtener.2017.07.014

18. R. Long, J. Liu, O. V. Prezhdo, Unravelling the effects of grain boundary and chemical doping on electron–hole recombination in $CH_3NH_3PbI_3$ perovskite by time-domain atomistic simulation. *J. Am. Chem. Soc.* **138**, 3884–3890 (2016). doi:10.1021/jacs.6b00645 Medline

19. T. Niu, J. Lu, R. Munir, J. Li, D. Barrit, X. Zhang, H. Hu, Z. Yang, A. Amassian, K. Zhao, S. F. Liu, Stable High-Performance Perovskite Solar Cells via Grain Boundary Passivation. *Adv. Mater.* **30**, e1706576 (2018). doi:10.1002/adma.201706576 Medline

20. S. Jariwala, H. Sun, G. W. P. Adhyaksa, A. Lof, L. A. Muscarella, B. Ehrler, E. C. Garnett, D. S. Ginger, Local crystal misorientation influences non-radiative recombination in halide perovskites. *Joule* **3**, 3048–3060 (2019). doi:10.1016/j.joule.2019.09.001

21. C. L. Davies, J. Borchert, C. Q. Xia, R. L. Milot, H. Kraus, M. B. Johnston, L. M. Herz, Impact of the organic cation on the optoelectronic properties of formamidinium lead triiodide. *J. Phys. Chem. Lett.* **9**, 4502–4511 (2018). doi:10.1021/acs.jpclett.8b01628 Medline

22. S. K. Yadavalli, Z. Dai, M. Hu, Q. Dong, W. Li, Y. Zhou, R. Zia, N. P. Padture, Mechanisms of Exceptional Grain Growth and Stability in Formamidinium Lead Triiodide Thin Films for Perovskite Solar Cells. *Acta Mater.* **193**, 10–18 (2020). doi:10.1016/j.actamat.2020.03.036

23. A. Knight, L. M. Herz, Preventing phase segregation in mixed-halide perovskites: A perspective. *Energy Environ. Sci.* **13**, 2024–2046 (2020). doi:10.1039/D0EE00788A

24. O. Breitenstein, J. Rakotoniaina, M. H. Al Rifai, M. Werner, Shunt types in crystalline silicon solar cells. *Prog. Photovolt. Res. Appl.* **12**, 529–538 (2004). doi:10.1002/pip.544

25. A. Stoffers, B. Ziebarth, J. Barthel, O. Cojocaru-Mirédin, C. Elsässer, D. Raabe, Complex Nanotwin Substructure of an Asymmetric Σ9 Tilt Grain Boundary in a Silicon Polycrystal. *Phys. Rev. Lett.* **115**, 235502 (2015). doi:10.1103/PhysRevLett.115.235502 Medline

26. Y. Yu, D. Zhang, C. Kisielowski, L. Dou, N. Kornienko, Y. Bekenstein, A. B. Wong, A. P. Alivisatos, P. Yang, Atomic resolution imaging of halide perovskites. *Nano Lett.* **16**, 7530–7535 (2016). doi:10.1021/acs.nanolett.6b03331 Medline

27. D. Zhang, Y. Zhu, L. Liu, X. Ying, C.-E. Hsiung, R. Sougrat, K. Li, Y. Han, Atomic-resolution transmission electron microscopy of electron beam-sensitive crystalline materials. *Science* **359**, 675–679 (2018). doi:10.1126/science.aao0865 Medline

28. Y. Li, W. Zhou, Y. Li, W. Huang, Z. Zhang, G. Chen, H. Wang, G.-H. Wu, N. Rolston, R. Vila, W. Chiu, Y. Cui, Unravelling degradation mechanisms and atomic structure of organic-inorganic halide perovskites by cryo-EM. *Joule* **3**, 2854–2866 (2019). doi:10.1016/j.joule.2019.08.016

29. M. U. Rothmann, W. Li, Y. Zhu, A. Liu, Z. Ku, U. Bach, J. Etheridge, Y.-B. Cheng, Structural and chemical changes to $CH_3NH_3PbI_3$ induced by electron and gallium ion beams. *Adv. Mater.* **30**, e1800629 (2018). doi:10.1002/adma.201800629 Medline

30. S. Chen, X. Zhang, J. Zhao, Y. Zhang, G. Kong, Q. Li, N. Li, Y. Yu, N. Xu, J. Zhang, K. Liu, Q. Zhao, J. Cao, J. Feng, X. Li, J. Qi, D. Yu, J. Li, P. Gao, Atomic scale insights into structure instability and decomposition pathway of methylammonium lead iodide perovskite. *Nat. Commun.* **9**, 4807 (2018). doi:10.1038/s41467-018-07177-y Medline

31. R. Hooley, A. Brown, A. Kulak, F. Meldrum, R. Brydson, *J. Phys. Conf. Ser.* **902**, 012005 (2017).

32. K. B. Lohmann, J. B. Patel, M. U. Rothmann, C. Q. Xia, R. D. J. Oliver, L. M. Herz, H. J. Snaith, M. B. Johnston, Control over crystal size in vapor deposited metal-halide perovskite films. *ACS Energy Lett.* **5**, 710–717 (2020). doi:10.1021/acsenergylett.0c00183 Medline

33. J. Borchert, R. L. Milot, J. B. Patel, C. L. Davies, A. D. Wright, L. Martínez Maestro, H. J. Snaith, L. M. Herz, M. B. Johnston, Large-area, highly uniform evaporated formamidinium lead triiodide thin films for solar cells. *ACS Energy Lett.* **2**, 2799–2804 (2017). doi:10.1021/acsenergylett.7b00967

34. J. Gonnissen, A. De Backer, A. J. den Dekker, G. T. Martinez, A. Rosenauer, J. Sijbers, S. Van Aert, Optimal experimental design for the detection of light atoms from high-

resolution scanning transmission electron microscopy images. *Appl. Phys. Lett.* **105**, 063116 (2014). doi:10.1063/1.4892884

35. L. Oesinghaus, J. Schlipf, N. Giesbrecht, L. Song, Y. Hu, T. Bein, P. Docampo, P. Müller-Buschbaum, Toward tailored film morphologies: The origin of crystal orientation in hybrid perovskite thin films. *Adv. Mater. Interfaces* **3**, 1600403 (2016). doi:10.1002/admi.201600403

36. H. J. Jung, D. Kim, S. Kim, J. Park, V. P. Dravid, B. Shin, Stability of halide perovskite solar cell devices: In situ observation of oxygen diffusion under biasing. *Adv. Mater.* **30**, e1802769 (2018). doi:10.1002/adma.201802769 Medline

37. T. W. Kim, S. Uchida, T. Matsushita, L. Cojocaru, R. Jono, K. Kimura, D. Matsubara, M. Shirai, K. Ito, H. Matsumoto, T. Kondo, H. Segawa, Self-Organized Superlattice and Phase Coexistence inside Thin Film Organometal Halide Perovskite. *Adv. Mater.* **30**, 1705230 (2018). doi:10.1002/adma.201705230 Medline

38. Z. Chen, Z.-G. Gu, W.-Q. Fu, F. Wang, J. Zhang, A confined fabrication of perovskite quantum dots in oriented MOF thin film. *ACS Appl. Mater. Interfaces* **8**, 28737–28742 (2016). doi:10.1021/acsami.6b11712 Medline

39. M. Xiao, F. Huang, W. Huang, Y. Dkhissi, Y. Zhu, J. Etheridge, A. Gray-Weale, U. Bach, Y.-B. Cheng, L. Spiccia, A fast deposition-crystallization procedure for highly efficient lead iodide perovskite thin-film solar cells. *Angew. Chem.* **126**, 10056–10061 (2014). doi:10.1002/ange.201405334 Medline

40. Y. Zhou, H. Sternlicht, N. P. Padture, Transmission electron microscopy of halide perovskite materials and devices. *Joule* **3**, 641–661 (2019). doi:10.1016/j.joule.2018.12.011

41. J. Ran, O. Dyck, X. Wang, B. Yang, D. B. Geohegan, K. Xiao, Electron-Beam-Related Studies of Halide Perovskites: Challenges and Opportunities. *Adv. Energy Mater.* **10**, 1903191 (2020). doi:10.1002/aenm.201903191

42. R. F. Egerton, Radiation damage to organic and inorganic specimens in the TEM. *Micron* **119**, 72–87 (2019). doi:10.1016/j.micron.2019.01.005 Medline

43. R. F. Egerton, P. Li, M. Malac, Radiation damage in the TEM and SEM. *Micron* **35**, 399–409 (2004). doi:10.1016/j.micron.2004.02.003 Medline

44. P. A. Beckmann, A review of polytypism in lead iodide. *Cryst. Res. Technol.* **45**, 455–460 (2010). doi:10.1002/crat.201000066

45. H.-S. Duan, H. Zhou, Q. Chen, P. Sun, S. Luo, T.-B. Song, B. Bob, Y. Yang, The identification and characterization of defect states in hybrid organic-inorganic perovskite photovoltaics. *Phys. Chem. Chem. Phys.* **17**, 112–116 (2015). doi:10.1039/C4CP04479G Medline

46. X. Wen, Y. Feng, S. Huang, F. Huang, Y.-B. Cheng, M. Green, A. Ho-Baillie, Defect trapping states and charge carrier recombination in organic–inorganic halide perovskites. *J. Mater. Chem. C* **4**, 793–800 (2016). doi:10.1039/C5TC03109E

47. D. W. deQuilettes, S. M. Vorpahl, S. D. Stranks, H. Nagaoka, G. E. Eperon, M. E. Ziffer, H. J. Snaith, D. S. Ginger, Impact of microstructure on local carrier lifetime in perovskite solar cells. *Science* **348**, 683–686 (2015). doi:10.1126/science.aaa5333 Medline

48. Q. Chen, H. Zhou, T.-B. Song, S. Luo, Z. Hong, H.-S. Duan, L. Dou, Y. Liu, Y. Yang, Controllable self-induced passivation of hybrid lead iodide perovskites toward high performance solar cells. *Nano Lett.* **14**, 4158–4163 (2014). doi:10.1021/nl501838y Medline

49. Y. Shao, Z. Xiao, C. Bi, Y. Yuan, J. Huang, Origin and elimination of photocurrent hysteresis by fullerene passivation in $CH_3NH_3PbI_3$ planar heterojunction solar cells. *Nat. Commun.* **5**, 5784 (2014). doi:10.1038/ncomms6784 Medline

50. A. F. Castro-Méndez, J. Hidalgo, J. P. Correa-Baena, The role of grain boundaries in perovskite solar cells. *Adv. Energy Mater.* **9**, 1901489 (2019). doi:10.1002/aenm.201901489

51. J. M. Ball, A. Petrozza, Defects in perovskite-halides and their effects in solar cells. *Nat. Energy* **1**, 16149 (2016). doi:10.1038/nenergy.2016.149

52. A. Merdasa, M. Bag, Y. Tian, E. Källman, A. Dobrovolsky, I. G. Scheblykin, Super-resolution luminescence microspectroscopy reveals the mechanism of photoinduced degradation in $CH_3NH_3PbI_3$ perovskite nanocrystals. *J. Phys. Chem. C* **120**, 10711–10719 (2016). doi:10.1021/acs.jpcc.6b03512

53. C. Xiao, Z. Li, H. Guthrey, J. Moseley, Y. Yang, S. Wozny, H. Moutinho, B. To, J. J. Berry, B. Gorman, Y. Yan, K. Zhu, M. Al-Jassim, Mechanisms of Electron-Beam-Induced Damage in Perovskite Thin Films Revealed by Cathodoluminescence Spectroscopy. *J. Phys. Chem. C* **119**, 26904–26911 (2015). doi:10.1021/acs.jpcc.5b09698

54. J. B. Patel, Q. Lin, O. Zadvorna, C. L. Davies, L. M. Herz, M. B. Johnston, Photocurrent spectroscopy of perovskite solar cells over a wide temperature range from 15 to 350 K. *J. Phys. Chem. Lett.* **9**, 263–268 (2018). doi:10.1021/acs.jpclett.7b02935 Medline

55. J. D. Zook, Effects of grain boundaries in polycrystalline solar cells. *Appl. Phys. Lett.* **37**, 223–226 (1980). doi:10.1063/1.91832

56. F. Greuter, G. Blatter, Electrical properties of grain boundaries in polycrystalline compound semiconductors. *Semicond. Sci. Technol.* **5**, 111–137 (1990). doi:10.1088/0268-1242/5/2/001

57. J.-W. Lee, D.-H. Kim, H.-S. Kim, S.-W. Seo, S. M. Cho, N.-G. Park, Formamidinium and Cesium Hybridization for Photo- and Moisture-Stable Perovskite Solar Cell. *Adv. Energy Mater.* **5**, 1501310 (2015). doi:10.1002/aenm.201501310

58. L. Kimerling, H. Leamy, J. Patel, The electrical properties of stacking faults and precipitates in heat-treated dislocation-free Czochralski silicon. *Appl. Phys. Lett.* **30**, 217–219 (1977). doi:10.1063/1.89355

59. H. Sugimoto, M. Inoue, M. Tajima, A. Ogura, Y. Ohshita, Analysis of intra-grain defects in multicrystalline silicon wafers by photoluminescence mapping and spectroscopy. *Jpn. J. Appl. Phys.* **45**, L641–L643 (2006). doi:10.1143/JJAP.45.L641

60. J. Borchert, I. Levchuk, L. C. Snoek, M. U. Rothmann, R. Haver, H. J. Snaith, C. J. Brabec, L. M. Herz, M. B. Johnston, Impurity Tracking Enables Enhanced Control and Reproducibility of Hybrid Perovskite Vapor Deposition. *ACS Appl. Mater. Interfaces* **11**, 28851–28857 (2019). doi:10.1021/acsami.9b07619 Medline

61. R. C. Gonzalez, R. E. Woods, *Digital Image Processing* (Addison-Wesley, 1992).

62. E. J. Kirkland, B. Siegel, N. Uyeda, Y. Fujiyoshi, Improved high resolution image processing of bright field electron micrographs: II. Experiment. *Ultramicroscopy* **17**, 87–103 (1985). doi:10.1016/0304-3991(85)90002-6

63. X. Pan, W. D. Kaplan, M. Rühle, R. E. Newnham, Quantitative comparison of transmission electron microscopy techniques for the study of localized ordering on a nanoscale. *J. Am. Ceram. Soc.* **81**, 597–605 (1998). doi:10.1111/j.1151-2916.1998.tb02379.x

64. L. J. Allen, A. J. D'Alfonso, S. D. Findlay, Modelling the inelastic scattering of fast electrons. *Ultramicroscopy* **151**, 11–22 (2015). doi:10.1016/j.ultramic.2014.10.011 Medline

65. H. Brown, http://tcmp.ph.unimelb.edu.au/mustem/muSTEM.html.

66. M. T. Weller, O. J. Weber, P. F. Henry, A. M. Di Pumpo, T. C. Hansen, Complete structure and cation orientation in the perovskite photovoltaic methylammonium lead iodide between 100 and 352 K. *Chem. Commun.* **51**, 4180–4183 (2015). doi:10.1039/C4CC09944C Medline

67. J. Peters, https://jjppeters.github.io/Strainpp/.

68. M. J. Hÿtch, E. Snoeck, R. Kilaas, Quantitative measurement of displacement and strain fields from HREM micrographs. *Ultramicroscopy* **74**, 131–146 (1998). doi:10.1016/S0304-3991(98)00035-7